scientific reports

Check for updates

OPEN

# Epitaxial lift-off of freestanding (011) and (111) $SrRuO_3$ thin films using a water sacrificial layer

Phu T. P. Le, Johan E. ten Elshof & Gertjan Koster✉

**Two-dimensional freestanding thin films of single crystalline oxide perovskites are expected to have great potential in integration of new features to the current Si-based technology. Here, we showed the ability to create freestanding single crystalline (011)- and (111)-oriented $SrRuO_3$ thin films using $Sr_3Al_2O_6$ water-sacrificial layer. The epitaxial $Sr_3Al_2O_6$(011) and $Sr_3Al_2O_6$(111) layers were realized on $SrTiO_3$(011) and $SrTiO_3$(111), respectively. Subsequently, $SrRuO_3$ films were epitaxially grown on these sacrificial layers. The freestanding single crystalline $SrRuO_3(011)_{pc}$ and $SrRuO_3(111)_{pc}$ films were successfully transferred on Si substrates, demonstrating possibilities to transfer desirable oriented oxide perovskite films on Si and arbitrary substrates.**

The integration of transition metal oxide (TMO) thin films and their heterostructures on Si are promising to provide new exciting features in applications of electronics, photonics, sensors, solid state lightning, microelectromechanical systems and so on, because of TMOs' rich physical properties[1–4]. The introduction of a buffer layer $SrTiO_3$(001) (STO) on Si(001) has triggered the development of epitaxial growth of oxide perovskites on Si(001)[5]. Furthermore, efforts have been made to epitaxially grow $(La_xY_{1-x})_2O_3$ and $Sc_2O_3$ buffer layers on Si(111)[6,7]. However, the introduction of buffer layers on Si suffers from complexities due to the reduction reaction and interdiffusion between oxides and Si at the interface while retaining the epitaxial relationship[8–10]. Alternatively, oxide nanosheets have been considered as crystalline templates to bridge TMOs and Si[11,12]. Although various TMO thin films have been directed in single out-of-plane orientation using oxide nanosheets[12–14], true epitaxy has not been achieved over the large scale on Si substrates yet.

Recently, the epitaxial lift-off technique that uses a sacrificial layer has emerged to prepare freestanding films of single crystalline TMOs, which can be transferred onto Si substrates[15–18]. The sacrificial layer acts as a crystallographic template to direct the epitaxial growth of TMO thin films, while it should be selectively removable using a chemical etchant without degrading the properties of the TMO thin films. MgO, $La_{0.7}Sr_{0.3}MnO_3$ and $Sr_3Al_2O_6$ (SAO) have primarily served as sacrificial layers to prepare freestanding TMO thin films thanks to their removability and epitaxial growth on single crystal substrates[15–17]. In addition to the compatible crystal structure of the oxide perovskites, the SAO sacrificial layer can be etched away using water, reducing contaminants and keeping the high-quality of oxide perovskite thin films[17].

Various freestanding oxide perovskites with (001) orientation releasing from SAO sacrificial layers have been fabricated and their properties have been studied[19–22]. The other (011) and (111) orientations also offer the ability to control the physical properties of oxide perovskites. For instance, with a thickness of 3 to 12 nm on $LaAlO_3$ substrates, $La_{0.67}Sr_{0.33}MnO_3$(001) was insulating while $La_{0.67}Sr_{0.33}MnO_3$ (011) was metallic[23]. The magnetic properties of several manganites were more enhanced in (011) than in (001) orientation[24,25]. The crystal structure of oxide perovskites can be regarded as buckled honeycomb-liked lattices in the [111] direction, which is a prerequisite for accessing many quantum phenomena, for example 2-dimensional (2D) topological insulators and the quantum anomalous Hall state[26–28]. Therefore, freestanding oxide perovskites with (011) and (111) orientations would add new features to Si. Furthermore, the metallic itinerant ferromagnetic $SrRuO_3$ (SRO) is a viable starting point for the growth of all oxide heterostructures thanks to its highly chemical and thermal stability[29–32]. In this study, the epitaxial growth of the SAO sacrificial layers on STO(011) and STO(111) orientations were realized using pulsed laser deposition (PLD). Subsequently, SRO films were epitaxially grown on SAO/STO heterostructures. The freestanding films of single crystalline $SRO(011)_{pc}$ and $SRO(111)_{pc}$, where $_{pc}$ stands for pseudocubic, were successfully transferred onto Si substrates. Before the epitaxial lift-off, large magnetic moments of 3.2 $\mu_B/Ru^{4+}$ and 3.5 $\mu_B/Ru^{4+}$ for $SRO(011)_{pc}$ and $SRO(111)_{pc}$ films were observed, suggesting $Ru^{4+}$ in the mixed state of low- and high-spin states and high-spin state, respectively. In contrast, the transferred

MESA+ Institute for Nanotechnology, University of Twente, P.O. Box 217, 7500 AE Enschede, The Netherlands. ✉email: g.koster@utwente.nl

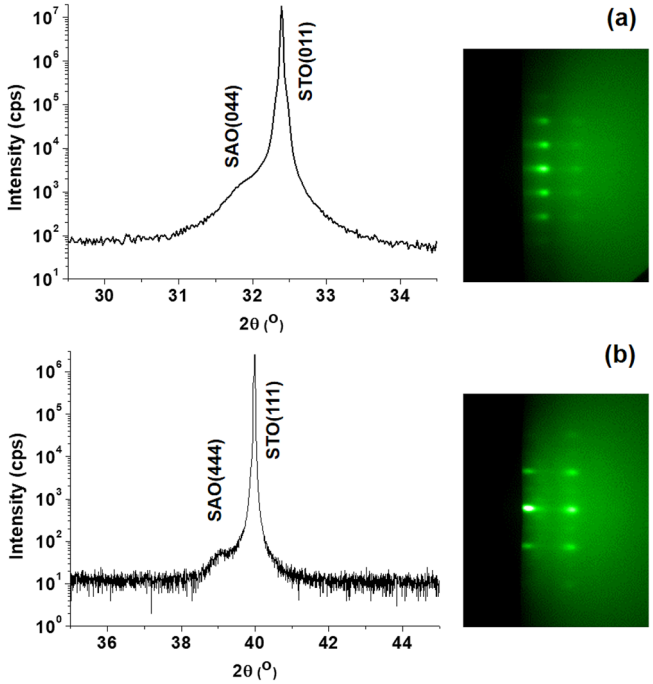


**Figure 1.** Epitaxial growth of SAO on STO(011) and STO(111) substrates. Panel (**a**) and (**b**) show XRD patterns of 100 nm SAO layers on STO(011) and STO(111) substrates, respectively, with capping STO layers. On the right-hand side, the spotty RHEED patterns of SAO layers were recorded along the [01-1] direction.

$SRO(011)_{pc}$ $SRO(111)_{pc}$ films showed a magnetic moment of 1.0 $\mu_B/Ru^{4+}$ and 1.7 $\mu_B/Ru^{4+}$, respectively, which resulted from the low-spin state of $Ru^{4+}$.

## Results and discussion

Figure 1 shows X-ray diffraction (XRD) patterns of 100 nm SAO films on STO(011) and STO(111) substrates and the corresponding reflection high-energy electron diffraction (RHEED) patterns of the SAO films (see Supplementary Figure S1 for the full scan XRD from 20° to 90°). The peak positions of SAO films at 31.87° and 39.10° matched with the bulk values of the SAO(044) and SAO(444) reflections, respectively, and the clear spotty RHEED patterns, which were recorded along the [01-1] direction of STO(011) and STO(111), indicated single crystalline nature of SAO films. The crystal structure of SAO has been described as a superstructure of 64 cubic perovskite units, in which the unit formula $ABO_3$ is $(Sr_{7/8}\square_{1/8})(Sr_{1/4}Al_{3/4})(O_{3/4}\square_{1/4})_3$ with vacancies at A and O positions[33]. Taking domain matching and the 2D symmetry of the crystal planes between SAO and STO into account, the epitaxial growth of SAO(011) and SAO(111) can be realized on STO(011) and STO(111), respectively, with a lattice mismatch of 1.43%.

In Fig. 2a and b, the 2θ-ω XRD patterns of SRO grown on SAO(011) and SAO(111), respectively, only showed peaks originating from the STO substrates. SAO(044) and SAO(444) peaks were not resolved in these XRD patterns probably because the SAO layers were thin, about 9.4 nm. However, the spotty and streaky RHEED patterns, which were recorded along the [01-1] direction of SRO grown on SAO(011) and SAO(111), indicated well-crystallized SRO films. It is worth mentioning that SRO films were directly grown on STO(011) and STO(111) substrates under the same growth condition of SRO layers in SRO/SAO/STO samples, $SRO(011)_{pc}$ and $SRO(111)_{pc}$ reflections were clearly observed (see Supplementary Figure S2). With regard to $SRO(011)_{pc}$/SAO(011)/STO(011), the reciprocal space map (RSM) around the STO(031) reflection (Fig. 2c) showed that $SRO(011)_{pc}$ was not fully strained to the STO(011) substrate. The $SRO(011)_{pc}$ film had $d_{(011)} = 2.768$ Å, which was close to $d_{(011)} = 2.762$ Å of the STO substrate, and that was why the $SRO(011)_{pc}$ peaks were not observed in Fig. 2a. Meanwhile, the RSM of $SRO(111)_{pc}$/SAO(111)/STO(111) (Fig. 2d) only showed a STO(231) peak. The $SRO(111)_{pc}$ reflections were not resolved probably because its (111) reflections were too close to those of STO(111) due to the insertion of the SAO(111) layer and its peak intensity was quite low compared to that of STO(111). The temperature-dependent resistivities of $SRO(011)_{pc}$/SAO(011)/STO(011) and $SRO(111)_{pc}$/SAO(111)/STO(111) are shown Fig. 2e. Both samples exhibited metallic behavior with a typical kink, which is caused by the ferromagnetic transition of SRO. The transition temperatures $T_c$ were 155 K and 154 K for $SRO(011)_{pc}$/SAO(011)/STO(011) and $SRO(111)_{pc}$/SAO(111)/STO(111), respectively, which are lower than the $T_c$ of bulk SRO, 160 K. This indicates that the SRO films were partially strained by the substrates[29]. While the residual resistivity ratio, $\rho_{300\,K}/\rho_{2\,K}$, of $SRO(011)_{pc}$ of 3.6 was better than the ratio 3.0 of $SRO(111)_{pc}$, the resistivity of $SRO(011)_{pc}$ was much higher than that of $SRO(111)_{pc}$. The reported residual resistivity ratios were in good agreement with other high-quality single crystalline SRO thin films by pulsed laser deposition[34,35]. Ning et al. showed that below 50 nm, the resistivity of $SRO(011)_{pc}$ was higher than that of $SRO(111)_{pc}$ on STO substrates because of the microstructure

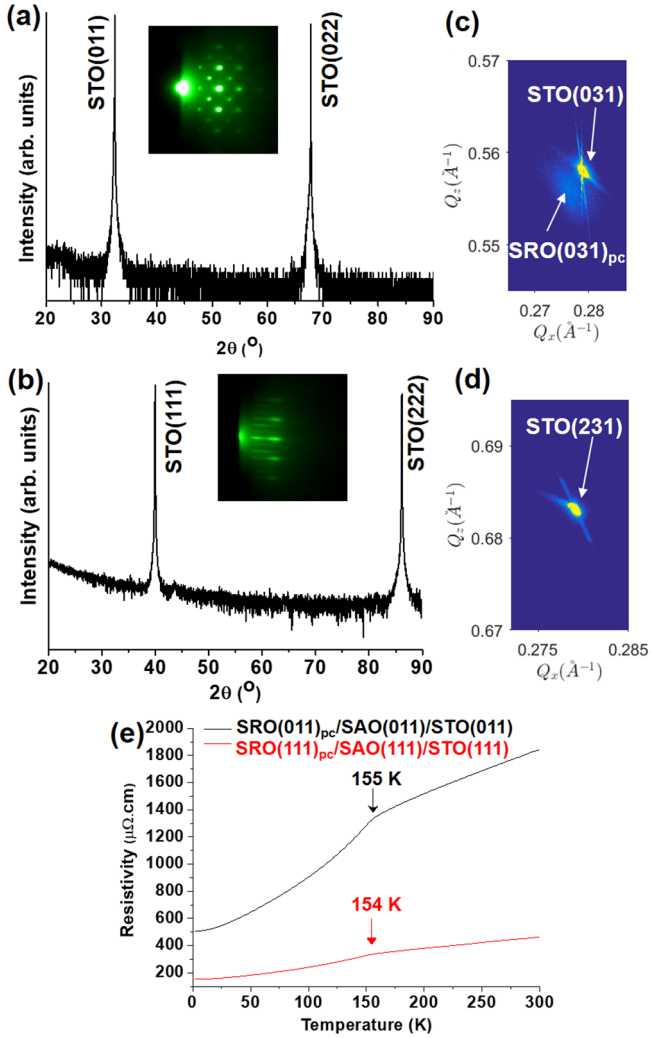


**Figure 2.** Identification of SRO films on sacrificial SAO layers. Panel (**a**) and (**b**) show that the XRD patterns of $SRO(011)_{pc}$/SAO(011)/STO(011) and $SRO(111)_{pc}$/SAO(111)/STO(111), respectively, could not resolve the reflections of SRO and SAO probably because the their reflections were close to those of STO and their intensities were much weaker than that of STO. The insets show clear spotty and streaky RHEED patterns, which were taken along the [01-1] direction of $SRO(011)_{pc}$ and $SRO(111)_{pc}$ films, respectively, indicating well-crystallized single phase SRO films. RSM around the STO(031) reflection (**c**) indicated that the $SRO(011)_{pc}$ film was not fully strained by the STO(011) substrate, while RSM around the STO(231) reflection (**d**) did not resolve the SRO(231) reflection of the $SRO(111)_{pc}$ film. The transport measurements (**e**) of $SRO(011)_{pc}$/SAO(011)/STO(011) and $SRO(111)_{pc}$/SAO(111)/STO(111) exhibited characteristic behavior of SRO films.

difference between columnar $SRO(011)_{pc}$ and dense $SRO(111)_{pc}$ films[36]. That can explain the higher resistivity of $SRO(011)_{pc}$ compared to that of $SRO(111)_{pc}$ on SAO/STO as we observed the microstructure differences in their RHEED patterns at the initial and final stages of SRO depositions (see Supplementary Figure S3) as well as their surface morphologies (see Supplementary Figure S4).

The SRO films were completely lifted off from the STO substrates (Fig. 3). However, the transfer process of SRO films onto Si(001) substrates resulted in cracks and some areas without SRO films. The film thicknesses were 37 nm and 24 nm for the transferred $SRO(011)_{pc}$ and $SRO(111)_{pc}$ films, respectively. The surface morphology of SRO films remained unchanged after the epitaxial lift-off and transfer processes (see Supplementary Figure S4).

The transferred $SRO(011)_{pc}$ on Si(001) substrates clearly showed the reflections of $SRO(011)_{pc}$ and $SRO(022)_{pc}$ at 32.25° and 67.49°, respectively, in the 2θ-ω scan (Fig. 4a) and the reflection of $SRO(031)_{pc}$ in the RSM (Fig. 4b). Similarly, the $SRO(222)_{pc}$ reflection was at 85.67° in the 2θ-ω scan (Fig. 4c) and the reflection of $SRO(231)_{pc}$, which was not resolved in the RSM of $SRO(111)_{pc}$/SAO(111)/STO(111), was observed in the RSM (Fig. 4d) for the transferred $SRO(111)_{pc}$ on Si(001) thanks to the separation with the reflections of the Si(001) substrate. The lattice constants $a_{pc}$ are 3.920 Å and 3.925 Å for transferred $SRO(011)_{pc}$ and $SRO(111)_{pc}$, respectively. Furthermore, Fig. 4e shows that the ϕ-scan of the in-plane reflection of $SRO(211)_{pc}$ of the transferred $SRO(011)_{pc}$ on Si(001) had 2 peaks, which were separated by 180°, consistent with the twofold symmetry of the $SRO(011)_{pc}$ film. Likewise, the ϕ-scan of the in-plane reflection of $SRO(240)_{pc}$ of the transferred $SRO(111)_{pc}$ in Fig. 4f obtained 6

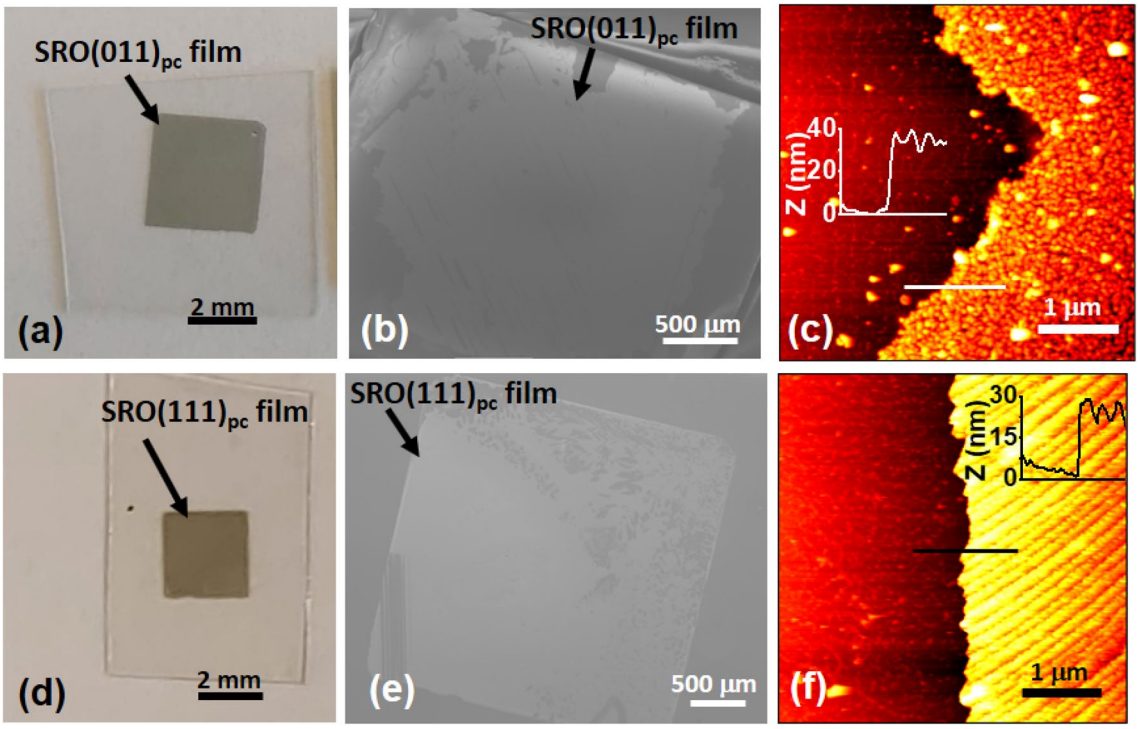


**Figure 3.** $SRO(011)_{pc}$ and $SRO(111)_{pc}$ films after the epitaxial lift-off and the transfer to Si(001) substrates. Millimeter-sized $SRO(011)_{pc}$ (**a**) and $SRO(111)_{pc}$ (**d**) films on the supporting polyethylene terephthalate (PET) substrates. SEM images of $SRO(011)_{pc}$ (**b**) and $SRO(111)_{pc}$ (**e**) on Si(001) substrates. Panel (**c**) and (**f**) show AFM data at the edges of $SRO(011)_{pc}$/Si(001) and $SRO(111)_{pc}$/Si(001), respectively. The insets show the thickness of transferred SRO films.

peaks, which were separated by 60° from each other, as one expected for the sixfold symmetry in the $SRO(111)_{pc}$ film. The in-plane direction between the transferred SRO films and Si(001) substrates was not coincident, simply because the transferred SRO films were arbitrarily placed on Si(001) substrates. Therefore, the SRO films were epitaxially grown on SAO/STO with the orientation of $(011)_{pc}$ and $(111)_{pc}$ and remained single crystalline films after the transfer to Si(001) substrates. Freestanding single crystalline STO(011) and STO(111) films were also lifted off from SAO/STO heterostructures (see Supplementary Figure S5).

Figure 5 shows magnetic hysteresis loops, which were measured with the applied magnetic field perpendicular to the film surface at 2 K, for $SRO(011)_{pc}$ and $SRO(111)_{pc}$ films before the epitaxial lift-off and after the transfer of SRO films on Si substrates. Before the epitaxial lift-off, the saturated magnetic moment was 3.2 $\mu_B/Ru^{4+}$ and 3.5 $\mu_B/Ru^{4+}$ for $SRO(011)_{pc}$ and $SRO(111)_{pc}$ films, respectively. Taken into account the change of SRO films' volume due to the transfer of SRO films on Si, the saturated magnetic moment was 1.0 $\mu_B/Ru^{4+}$ and 1.7 $\mu_B/Ru^{4+}$ for $SRO(011)_{pc}$ and $SRO(111)_{pc}$ films, respectively. With regard to SRO, it was suggested that the low-spin $Ru^{4+}$ state has a magnetic moment of 2 $\mu_B/Ru^{4+}$, while the high-spin one has 4 $\mu_B/Ru^{4+}$[34,36–40]. The bulk SRO showed 1.1–1.6 $\mu_B/Ru^{4+}$ in the low-spin state[40]. It has been experimentally observed that the high-spin state can be stabilized using epitaxial strain and the symmetry of the lattice distortion via substrates[34,36–39]. $SRO(111)_{pc}$ epitaxially grown on STO(111) adopted the high-spin state with the magnetic moment of 3.5–3.6 $\mu_B/Ru^{4+}$, while $SRO(011)_{pc}$ grown on STO(011) had a mixed state of low- and high-spin states with the magnetic moment of 3 $\mu_B/Ru^{4+}$[36,37]. Because the epitaxial lift-off of SRO films happened in pure deionized $H_2O$ at room temperature, SRO films are unlikely to have undergone chemical reactions, such as acid–base and redox reactions, with $H_2O$ that would have affected its composition and/or structure. The magnetic moment values of $SRO(111)_{pc}$ on SAO(111)/STO(111) suggest that the $SRO(111)_{pc}$ film has a high-spin state, and the transferred $SRO(111)_{pc}$ film on Si substrate adopts the low-spin state like bulk SRO, because it was not under any strain and not distorted by the weak Van der Waals bonds on the Si substrate. Similarly, the $SRO(011)_{pc}$ films would have a mixed state of high-spin and low-spin states and the low-spin state before epitaxial lift-off and after the transfer, respectively.

## Conclusions

In this study, we have shown freestanding single crystalline of $SrRuO_3$ films with (011) and (111) orientations were successfully synthesized using water-sacrificial SAO layers on single crystal STO substrates. The water-sacrificial SAO layers were epitaxially grown on STO(011) and STO(111) because of lattice mismatch of 1.43% and similar 2D symmetry of crystal planes. The single crystalline $(011)_{pc}$- and $(111)_{pc}$-oriented SRO films were successfully transferred on Si substrates. SRO films on SAO(011)/STO(011) and SAO(111)/STO(111) heterostructures showed enhanced magnetism of the high-spin state, whereas the transferred SRO films on Si showed

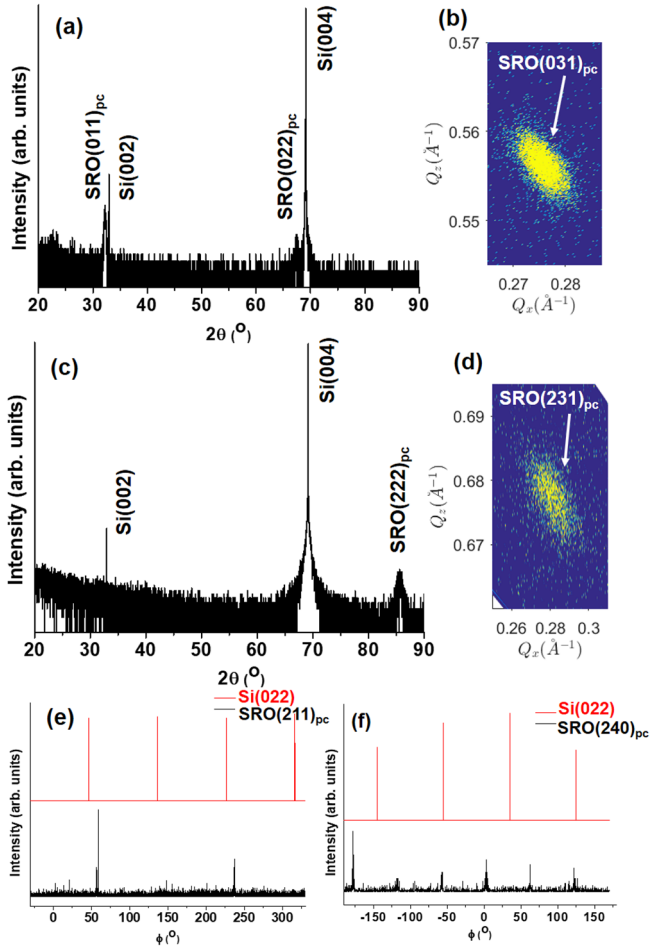


**Figure 4.** Single crystalline $SRO(011)_{pc}$ and $SRO(111)_{pc}$ films on Si(001). Clearly resolved reflections in 2θ-ω scans of $SRO(011)_{pc}$ (**a**) and $SRO(111)_{pc}$ (**c**) confirmed single oriented SRO films on Si(001) substrates. Panel (**b**) shows clear $SRO(031)_{pc}$ reflection of $SRO(011)_{pc}$ film in RMS, while panel (**d**) displays the $SRO(231)_{pc}$ reflection of $SRO(111)_{pc}$ film, which was not resolved when the film was on STO(111) substrate. The ϕ-scans reveal 2 peaks, which were separated by 180°, for the in-plane reflection $SRO(211)_{pc}$ of $SRO(011)_{pc}$ in panel (**e**) and 6 peaks, which were separated 60°, for the in-plane reflection $SRO(240)_{pc}$ of $SRO(111)_{pc}$ films in panel (**f**).

bulk-like magnetism of the low-spin state. This study demonstrates the possibility to obtain single crystalline oxide perovskite films with desirable orientation on arbitrary substrates.

## Methods

Well-defined atomically flat STO substrates were obtained by treating STO with buffered hydrogen fluoride solution and then thermal annealing as described elsewhere[41,42]. PLD was performed in a vacuum system with a base pressure of $2 \times 10^{-8}$ mbar, equipped with an in situ RHEED and a KrF excimer laser of 248 nm (COMPexPro from Coherent Inc.). The central part of the laser beam was selected with a mask and focused on polycrystalline SAO, SRO, and single crystal STO targets. The substrate temperature 700 °C, laser repletion rate 1 Hz, spot size 1.8 $mm^2$ and substrate-target distance 50 mm were the same for the growth of SAO, SRO and STO layers. Laser energy density and oxygen pressure were 1.25 J $cm^{-2}$ and $10^{-3}$ mbar for SAO, 1.3 J $cm^{-2}$ and $10^{-2}$ mbar for STO, and 2.1 J $cm^{-2}$ and $8 \times 10^{-3}$ mbar for SRO. After deposition, the samples were cooled down to room temperature at a maximum rate of 20 °C $min^{-1}$ at the deposition pressure for STO/SAO/STO heterostructures and at 100 mbar oxygen pressure for SRO/SAO/STO heterostructures. The growth rate was 1.88 nm per 100 pulses for SAO(011) and SAO(111) (see Supplementary Figure S6). The transfer of epitaxial films from SAO water-sacrificial layers on supporting substrates was done as described elsewhere[17,43].

The crystal structure of samples was analyzed using PANalytical X'Pert Pro with the Inc. beam Monochr. 4xGe220 Cu asym. LF monochromator to select Cu $K\alpha_1$ radiation. Scanning electron microscope (SEM) (Jeol JSM-6490) was used to acquire the images of the transferred SRO films on Si substrates in order to calculate the transferred film area based on the contrast between SRO and Si. Surface morphologies of samples were investigated using atomic force microscopy (AFM), Bruker Dimension ICON, operating in tapping mode and analyzed by Gwyddion software[44]. The transport measurements were performed in the four-probe Van der Pauw

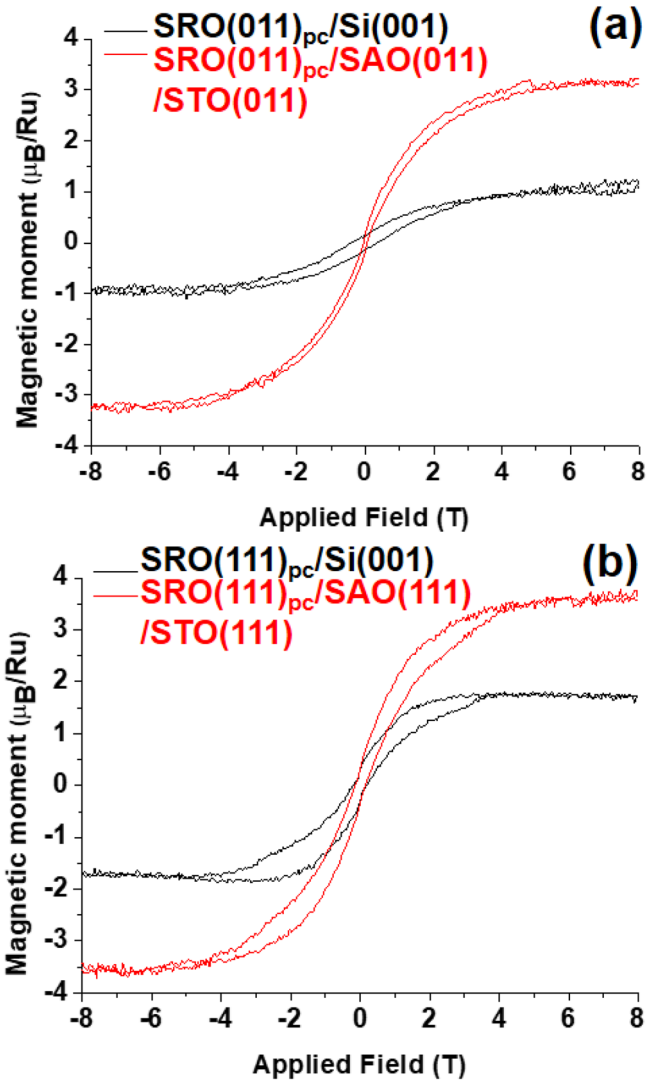


**Figure 5.** Magnetic hysteresis loops measured with the applied magnetic field perpendicular to the film surface of $SRO(011)_{pc}$ (**a**) and $SRO(111)_{pc}$ (**b**) films at 2 K. The saturated magnetic moment for $Ru^{4+}$ was 3.2 $\mu_B/Ru^{4+}$ and 3.5 $\mu_B/Ru^{4+}$ for the $SRO(011)_{pc}$ and $SRO(111)_{pc}$ films, respectively, when they were on SAO/STO heterostructures, probably because of the presence of the $Ru^{4+}$ high-spin state. After the transfer onto Si substrates, $SRO(011)_{pc}$ and $SRO(111)_{pc}$ films had 1.0 $\mu_B/Ru^{4+}$ and 1.7 $\mu_B/Ru^{4+}$, respectively, as their crystal structure were relaxed to the bulk SRO from epitaxial strain and lattice distortion by SAO/STO heterostructures.

configuration and the magnetic properties were measured with the magnetic field perpendicular to the film surface using vibrating sample magnetometry in a Quantum Design Physical Properties Measurement System.

Received: 20 April 2021; Accepted: 31 May 2021
Published online: 14 June 2021

## References

1. Eerenstein, W., Mathur, N. D. & Scott, J. F. Multiferroic and magnetoelectric materials. *Nature* **442**, 759–765 (2006).
2. Rao, C. N. R. Transition metal oxides. *Annu. Rev. Phys. Chem.* **40**, 291–326 (1989).
3. Demkov, A. A. & Posadas, A. B. *Integration of Functional Oxides with Semiconductors* (Springer, New York, 2014). https://doi.org/10.1007/978-1-4614-9320-4.
4. Manipatruni, S., Nikonov, D. E. & Young, I. A. Beyond CMOS computing with spin and polarization. *Nat. Phys.* **14**, 338–343 (2018).
5. McKee, R. A., Walker, F. J. & Chisholm, M. F. Crystalline Oxides on Silicon: The First Five Monolayers. *Phys. Rev. Lett.* **81**, 3014–3017 (1998).
6. Guha, S., Bojarczuk, N. A. & Narayanan, V. Lattice-matched, epitaxial, silicon-insulating lanthanum yttrium oxide heterostructures. *Appl. Phys. Lett.* **80**, 766–768 (2002).
7. Klenov, D. O., Edge, L. F., Schlom, D. G. & Stemmer, S. Extended defects in epitaxial $Sc_2O_3$ films grown on (111) Si. *Appl. Phys. Lett.* **86**, 051901 (2005).

8. Shutthanandan, V. *et al.* Direct observation of atomic disordering at the SrTiO3/Si interface due to oxygen diffusion. *Appl. Phys. Lett.* **80**, 1803 (2002).
9. Gu, X. *et al.* Commercial molecular beam epitaxy production of high quality SrTiO3 on large diameter Si substrates. *J. Vac. Sci. Technol. B Microelectron. Nanometer Struct. Process. Meas. Phenom.* **27**, 1195–1199 (2009).
10. Reiner, J. W. *et al.* Crystalline oxides on silicon. *Adv. Mater.* **22**, 2919–2938 (2010).
11. Timmerman, M. A., Xia, R., Le, P. T. P., Wang, Y. & ten Elshof, J. E. Metal oxide nanosheets as 2D building blocks for the design of novel materials. *Chem. Eur. J.* **26**, 9084–9098 (2020).
12. Shibata, T. *et al.* Versatile van der Waals epitaxy-like growth of crystal films using two-dimensional nanosheets as a seed layer: Orientation tuning of SrTiO3 films along three important axes on glass substrates. *J. Mater. Chem. C* **2**, 441–449 (2013).
13. Le, P. T. P. *et al.* Tailoring vanadium dioxide film orientation using nanosheets: A combined microscopy, diffraction, transport, and soft X-ray in transmission study. *Adv. Funct. Mater.* **30**, 1900028 (2020).
14. Nijland, M. *et al.* Epitaxy on demand. *Adv. Funct. Mater.* **25**, 5140–5148 (2015).
15. Paskiewicz, D. M., Sichel-Tissot, R., Karapetrova, E., Stan, L. & Fong, D. D. Single-crystalline SrRuO3 nanomembranes: A platform for flexible oxide electronics. *Nano Lett.* **16**, 534–542 (2016).
16. Bakaul, S. R. *et al.* Single crystal functional oxides on silicon. *Nat. Commun.* **7**, 1–5 (2016).
17. Lu, D. *et al.* Synthesis of freestanding single-crystal perovskite films and heterostructures by etching of sacrificial water-soluble layers. *Nat. Mater.* **15**, 1255–1260 (2016).
18. Gu, K. *et al.* Simple method to obtain large-size single-crystalline oxide sheets. *Adv. Funct. Mater.* **30**, 2001236 (2020).
19. Hong, S. S. *et al.* Extreme tensile strain states in La0.7Ca0.3MnO3 membranes. *Science* **368**, 71–76 (2020).
20. Han, L. *et al.* Giant uniaxial strain ferroelectric domain tuning in freestanding PbTiO3 films. *Adv. Mater. Interfaces* **7**, 1901604 (2020).
21. Ji, D. *et al.* Freestanding crystalline oxide perovskites down to the monolayer limit. *Nature* **570**, 87–90 (2019).
22. Singh, P. *et al.* Large-area crystalline BaSnO3 membranes with high electron mobilities. *ACS Appl. Electron. Mater.* **1**, 1269–1274 (2019).
23. Tebano, A., Orsini, A., Di Castro, D., Medaglia, P. G. & Balestrino, G. Interplay between crystallographic orientation and electric transport properties in La2/3Sr1/3MnO3 films. *Appl. Phys. Lett.* **96**, 092505 (2010).
24. Infante, I. C. *et al.* Elastic and orbital effects on thickness-dependent properties of manganite thin films. *Phys. Rev. B* **76**, 224415 (2007).
25. Minohara, M., Furukawa, Y., Yasuhara, R., Kumigashira, H. & Oshima, M. Orientation dependence of the Schottky barrier height for La0.6Sr0.4MnO3/SrTiO3 heterojunctions. *Appl. Phys. Lett.* **94**, 242106 (2009).
26. Okamoto, S. & Xiao, D. Transition-metal oxide (111) bilayers. *J. Phys. Soc. Jpn.* **87**, 041006 (2018).
27. Si, L. *et al.* Quantum anomalous hall state in ferromagnetic SrRuO3 (111) bilayers. *Phys. Rev. Lett.* **119**, 026402 (2017).
28. Wang, Y., Wang, Z., Fang, Z. & Dai, X. Interaction-induced quantum anomalous Hall phase in (111) bilayer of LaCoO3. *Phys. Rev. B* **91**, 125139 (2015).
29. Koster, G. *et al.* Structure, physical properties, and applications of SrRuO3 thin films. *Rev. Mod. Phys.* **84**, 253–298 (2012).
30. Lee, B., Kwon, O.-U., Shin, R. H., Jo, W. & Jung, C. U. Ferromagnetism and Ru-Ru distance in SrRuO3 thin film grown on SrTiO3 (111) substrate. *Nanoscale Res. Lett.* **9**, 8 (2014).
31. Woo, S. *et al.* Enhanced magnetic and thermoelectric properties in epitaxial polycrystalline SrRuO3 thin films. *Nanoscale* **10**, 4377–4384 (2018).
32. Seo, H. I. *et al.* Crystalline symmetry-dependent magnon formation in the itinerant ferromagnet SrRuO3. *Phys. Rev. B* **103**, 045104 (2021).
33. Alonso, J. A., Rasines, I. & Soubeyroux, J. L. Tristrontium dialuminum hexaoxide: an intricate superstructure of perovskite. *Inorg. Chem.* **29**, 4768–4771 (1990).
34. Grutter, A. J., Wong, F. J., Arenholz, E., Vailionis, A. & Suzuki, Y. Evidence of high-spin Ru and universal magnetic anisotropy in SrRuO3 thin films. *Phys. Rev. B* **85**, 134429 (2012).
35. Jia, Q. X. *et al.* Characteristics of conductive SrRuO3 thin films with different microstructures. *J. Mater. Res.* **11**, 2263–2268 (1996).
36. Ning, X. K., Wang, Z. J. & Zhang, Z. D. Anisotropy of electrical and magnetic transport properties of epitaxial SrRuO3 thin films. *J. Appl. Phys.* **117**, 093907 (2015).
37. Grutter, A. *et al.* Enhanced magnetism in epitaxial SrRuO3 thin films. *Appl. Phys. Lett.* **96**, 082509 (2010).
38. Wang, X. W. *et al.* Magnetic anisotropy and transport properties of 70 nm SrRuO3 films grown on different substrates. *J. Appl. Phys.* **109**, 07D707 (2011).
39. Liu, J. *et al.* Mechanically tunable magnetic properties of flexible SrRuO3 epitaxial thin films on mica substrates. *Adv. Electron. Mater.* **4**, 1700522 (2018).
40. Allen, P. B. *et al.* Transport properties, thermodynamic properties, and electronic structure of SrRuO3. *Phys. Rev. B* **53**, 4393–4398 (1996).
41. Koster, G., Kropman, B. L., Rijnders, G. J. H. M., Blank, D. H. A. & Rogalla, H. Quasi-ideal strontium titanate crystal surfaces through formation of strontium hydroxide. *Appl. Phys. Lett.* **73**, 2920–2922 (1998).
42. Biswas, A. *et al.* Universal Ti-rich termination of atomically flat SrTiO3 (001), (110), and (111) surfaces. *Appl. Phys. Lett.* **98**, 051904 (2011).
43. Chen, X.-D. *et al.* High-quality and efficient transfer of large-area graphene films onto different substrates. *Carbon* **56**, 271–278 (2013).
44. Nečas, D. & Klapetek, P. Gwyddion: An open-source software for SPM data analysis. *Cent. Eur. J. Phys.* **10**, 181–188 (2012).


## Acknowledgements

P.T.P.L thanks Minh D. Nguyen for providing cut Si substrates. P.T.P.L, J.E.tE and G.K acknowledge the Netherlands Organisation for Scientific Research (NWO)/CW ECHO grant ECHO.15.CM2.043.

## Author contributions

P.T.P.L, J.E.tE and G.K conceived the concept. P.T.P.L conducted the experiments. J.E.tE and G.K supervised the experiments. The manuscript was written through contributions of all authors. All authors have given approval to the final version of the manuscript.

## Competing interests

The authors declare no competing interests.

## Additional information

**Supplementary Information** The online version contains supplementary material available at https://doi.org/10.1038/s41598-021-91848-2.

**Correspondence** and requests for materials should be addressed to G.K.